Theoretical Analysis of Tunnel-Injected Sub-300 nm AlGaN Laser Diodes

Riazul Arefin, Weicheng You, Sujit H. Ramachandra, Syed M. N. Hasan, Hyemin Jung, Mohammad Awwad, and Shamsul Arafin, *Senior Member, IEEE*

***Abstract*— Electrically-pumped AlGaN-based edge-emitting laser diodes with a buried tunnel junction (TJ) for sub-300 nm emission are designed in this paper. Hole injection is one of the major concerns for the design of ultraviolet (UV) lasers based on this material system. The use of a low-resistive TJ as an intracavity contact within the devices will offer an opportunity to replace highly resistive *p*-type AlGaN-based cladding and contact layers by their *n*-doped counterparts. This advanced polarization-engineered interband TJs will lead to improved hole injection and a significantly reduced threshold voltage. The thermal properties of the tunnel-injected devices are thoroughly studied theoretically. For the demonstration of continuous-wave operating lasers, possible improvements in terms of better thermal management of the device are also discussed. Our improved design allows CW-operating AlGaN lasers with a threshold current density of <8 kA/cm^2 and maximum optical output power of > 220 mW, yielding a wall-plug efficiency of > 2.8%.**

***Index Terms*— UV-B laser, tunnel junction, AlGaN, absorption coefficient, thermal impedance.**

I. Introduction

ELECTRICALLY-PUMPED (EP) and continuous-wave (CW) operating AlGaN-based diode lasers in the UV-B (320–280 nm) and UV-C (280–200 nm) wavelength regimes are currently gaining significant research interests. This is due to a wide range of emerging applications including phototherapy in the medical sector, plant growth lighting, water sterilization, trace gas sensing, curing polymers, and stimulating the formation of anti-cancerogenic substances [1], [2]. In particular, UV-B lasers are useful for data storage, decontamination, precision manufacturing, real-time medical diagnostics, as well as chemical and biological identification using Raman spectroscopy [3]. Most importantly, these lasers are recently found to be useful for sterilizing surfaces or objects, as one of the precautionary steps to prevent the global spread of the coronavirus (COVID-19) [4].

According to the Ultraviolet Germicidal Irradiation Handbook, one minute of UV-B and -C light exposure sterilizes more than 90% of the coronavirus. Tests conducted by Chinese agencies on appliances equipped with UV-light source sterilization have demonstrated a 97% reduction in airborne virus particles [4]. Arguably, some of these highly demanding applications could be enabled by light emitting diodes (LEDs) in this wavelength regime. However, energy-inefficient UV-B/C LEDs achieved to-date are large, complicated, and expensive, which essentially limits their applicability in these key areas. Moreover, light extraction and efficiency-droop constraints in LEDs can easily be alleviated by lasers [5]. Hence, a foundation of all these applications points towards the development of high-efficiency and high-power AlGaN-based lasers emitting in the UV-B and UV-C spectral ranges.

The major challenges for EP AlGaN lasers are related to *p*-doping and hole injection due to extremely high ionization energy ($\geq$400 meV) of Mg acceptors in high-Al containing AlGaN layers. In addition, high hole effective masses ($>2m_e$) leads to highly resistive *p*-AlGaN layers, introducing challenges to making low-resistive *p*-contacts [6]. It is important to find a way of designing EP AlGaN-diode lasers with improved hole-injection, allowing all of these aforementioned difficulties to be bypassed. Techniques to overcome the issue of hole-injection include distributed polarization doping [7], short-period superlattice [8], and the introduction of tunnel junctions (TJs) [9] which have been adopted in proof-of-concept opto-electronic devices. This paper reports a detailed laser design methodology based on buried TJ as an intracavity contact which improves electrical properties while maintaining low optical losses. The key advantages of the TJ-based approach over conventional *p-i-n* diode-based designs are described in [6] and [9].

While GaN-based lasers have been demonstrated with excellent performance, achieving sub-300 nm UV lasers based on AlGaN is challenging. To our best knowledge, there are no EP UV-B lasers demonstrated to date. However, lasers with the emission wavelengths of 336 nm [10] and 342 nm [11], operating at pulsed threshold current densities of 17.6 kA/cm^2 and 8.7 kA/cm^2, respectively, were achieved mainly due to significant efforts in the past decade towards obtaining low defect density templates and good material quality through an optimized growth process. Unfortunately, very little success has been achieved in realizing shorter-wavelength UV laser diodes. Very recently, EP and room-temperature operating AlGaN-based UV-C lasers at record-short $\lambda = 271.8$ nm were reported, that operate at a pulsed threshold current density of 25 kA/cm^2 [7]. A distributed polarization doped cladding layer was employed to achieve good hole conductivity in the laser structures which exhibited a differential quantum efficiency of only 1.4%. We present a comprehensive design

Manuscript received May 28, 2020; revised August 6, 2020; accepted August 31, 2020. Date of publication September 3, 2020; date of current version September 21, 2020. *(Corresponding author: Shamsul Arafin.)*

The authors are with the Department of Electrical and Computer Engineering, The Ohio State University, Columbus, OH 43210 USA (e-mail: arafin.1@osu.edu).

Color versions of one or more of the figures in this article are available online at http://ieeexplore.ieee.org.

Digital Object Identifier 10.1109/JQE.2020.3021404

methodology of AlGaN-based lasers in this theoretical study which can be used as guidelines for realizing devices in this critical ultra-short wavelength regime.

This paper begins with a discussion on the theoretical calculations associated with the feasibility of the proposed TJ-based UV-B laser design. All the optical, electrical and thermal design issues of the lasers are first addressed. We then present simulation results of the TJ-injected devices to enable sufficient carrier injection, with a reasonable voltage drop to achieve EP lasing. The paper closes with concluding remarks on the proposed device design and possible path forward towards realizing highly-demanding UV-B lasers.

II. AlGaN Laser Structure

The Fabry–Pérot (FP) edge-emitting lasers designed in this study employs a first epitaxial 100 nm n^+-$Al_{0.72}GaN$ layer onto which an n-side contact can be defined. This layer is followed by a 450 nm n-$Al_{0.72}GaN$ cladding layer, a 112 nm $Al_{0.65}GaN$ n-waveguide layer and a multi-quantum well (MQW) active region for $\lambda = 290$ nm emission. An Mg-doped 18 nm-thick electron blocking layer (EBL) is then placed, which is deliberately p-doped to restrict most of the band offset to the conduction band. In other words, p-doping the EBL reduces the AlN/p-$Al_{0.65}GaN$ hetero-barrier for holes in the valence band, which results in improved hole injection. For further enhancement of the hole injection into the active region, the composition, thickness and hole concentration of the EBL are usually engineered to get rid of polarization-induced charges at both the last-quantum-barrier/p-AlN as well as p-AlN/p-waveguide interfaces.

Our design considers only a 10 nm p-waveguide layer on top of the EBL, which yields an asymmetric design as shown in Fig. 1. This can be understood by the p- and n-waveguide layers of unequal thicknesses, sandwiching the MQW-based active region. In other words, the structure utilizes the so-called 'offset quantum-well' (OQW) design, where the MQWs are intentionally placed on top of a relatively thicker n-$Al_{0.65}GaN$ waveguide layer. The design then employs p^+-AlGaN/i-GaN/n^+-AlGaN TJ layers, a 440 nm n^+-$Al_{0.65}GaN$ cladding layer, and a 40 nm reverse compositionally-graded heavily-doped (2×10^{19} cm^{-3}) n-AlGaN layer with an Al mole fraction from 72% to 15% in order to form a top p-side low-resistive ohmic contact. Due to the TJ, the top p-side contact is formed on the n^+-doped layer. It should be noted that the consideration of the TE-polarized emission at this wavelength regime can be justified by experimental evidence obtained from AlGaN MQW LEDs. It is found that such devices with wavelengths longer than 250 nm prefer strong TE-polarized emission irrespective of QW thicknesses [12].

A. Substrate Materials

For the UV-B or C optoelectronic devices, there are usually two common trends while selecting substrate materials. As a foreign substrate, sapphire (Al_2O_3) is still the most popular material for manufacturing low-cost UV devices. Optically-pumped AlGaN MQW lasers grown on sapphire

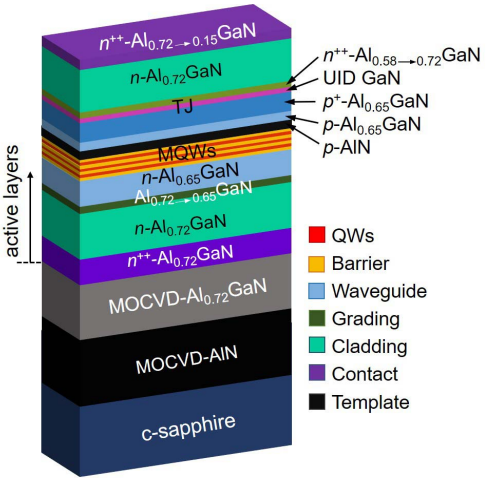

Fig. 1. A 3D schematic of the offset quantum well-based AlGaN laser structure with the buried TJ designed for an emission wavelength of 290 nm.

substrates emitting at UV-B and -C have already been demonstrated [13], [14]. The substrates can be prepared with a μm-thick metal-polar $Al_{0.72}GaN$ layer grown on AlN templates. A compressive strain between the AlN template and the thick n-$Al_{0.7}GaN$ film promotes complete relaxation. However, the efficiency in the devices fabricated on sapphire substrates is impacted by a high threading dislocation density (TDD) in the associated epitaxial layers [15]. For longer wavelength devices made on native substrates, TDDs are only on the order of $<10^4$ cm^{-2}. To obtain the TDDs on the same order, growing a few-micron-thick AlN template on the sapphire substrates is proven to be one of the most effective methods [16]. However, the AlN templates on sapphire usually suffer from defect densities in the range of 10^{11}-10^{12} cm^{-2} due to the higher order of lattice mismatch [16], [17].

Poor-quality thin AlN templates on sapphire are now commercially available. Such thin AlN-templates can be used to shorten the growth time prior to additional AlN growth towards obtaining high-quality AlN. In fact, to make the templates suitable for growing active layers and filter out the dislocations further in order to reduce the TDDs to $<10^9$ cm^{-2}, a thick AlN is usually grown on top of the substrate followed by downgrading the Al-composition to a target mole fraction. As an alternative to obtaining good-quality epi-ready substrate, single-crystal AlN bulk crystal offers two orders of magnitude lower TDDs than ultra-thick AlN/sapphire. Templates with a targeted Al-composition on AlN substrates provide low dislocation densities which are expected to provide a better quality of the active layers, yielding high-performance lasers [3], [18].

B. Growth Technology

The two most popular methods available for epitaxial growth of the tunnel-injected AlGaN laser structures are molecular beam epitaxy (MBE) and metalorganic chemical vapor deposition (MOCVD). Due to high growth-temperatures and -rates, MOCVD is superior to MBE for growing high-quality AlN templates. One can then grow laser materials by employing either of the growth techniques on top of such MOCVD-grown templates. Based on recent results, the

MOCVD-grown LEDs have shown better quantum efficiency in comparison to MBE-grown devices in the wavelengths of interest [19]. From a commercial standpoint, an all-MOCVD growth process is preferred since the entire epitaxial stack can be realized within one growth cycle in a commercial MOCVD environment. However, due to the use of buried TJs in the design, the MBE growth precedes the MOCVD process. This is because of the fact that MBE-growth offers both activation- and memory-effect-free structures for Mg-dopants as well as provides sharp doping profiles within TJs which is necessary for efficient tunneling.

One can also consider a hybrid growth scheme by which a base structure, containing all the layers up to an active region and the p^+-side of the TJ, is grown by MOCVD, and the remainder of the device including the n^+-side of TJs, n-cladding and n^+-contact layers can be overgrown during the second epitaxial growth by MBE. Hence, the hybrid MOCVD/MBE approach, comprised of an MOCVD-grown base structure with active region and MBE-grown TJs, may be one of the viable routes towards obtaining high performance UV-B/C lasers. Low-resistive MOCVD grown TJs have been demonstrated in LEDs [20]. However, the targeted operating current densities in such devices is relatively much lower ($\sim$20 A/cm^2) [21] than in lasers, questioning the efficacy of the MOCVD-TJs. At current densities of $>$1 kA/cm^2, the MOCVD grown TJs lead to higher voltage-drops compared to MBE grown ones [20], [22]. Thus, growing the samples in two steps brings in a trade-off between the process complexity/device cost and attainable device performance.

III. Optical Design

A. Mode Simulation

Using the complex refractive indices of the epitaxial layers, the two-dimensional (2D) transverse optical mode of a ridge waveguide laser was simulated. A 3D schematic of the shallow-ridge AlGaN lasers is presented in Fig. 2(a) while Fig. 2(b) shows the 1D optical intensity distribution of the fundamental transverse electric (TE) mode along with the corresponding refractive index profile. Given that the laser structure employs compressively-strained $Al_{0.5}Ga_{0.5}N$ MQWs, the consideration of TE mode dominant emissions can be justified [12]. In this configuration, the optical mode overlap with the QWs is not maximized. This design leads to a reduced overlap of this optical mode with the highly-absorbing TJ, placed a few tens of nanometers away from the active region. Such an asymmetric device design can greatly minimize the optical loss without significantly sacrificing the optical modal confinement of QWs. The close-up view of the optical intensity distribution near the active region, shown in Fig. 2(c), confirms the OQW design. The confinement factor Γ of several regions of the device is calculated in order to assess our optical design. Table I lists the Γ values in the important layers of the laser structure.

B. Optical Absorption in Polarization Engineered TJ

The TJs, being one of the critical components, require careful design and positioning within the laser device to minimize optical absorption loss without sacrificing electrical performance. In our case, the TJ is strategically placed on top of the thin p-waveguide layer, that allows a device structure with the least possible p-doped layers. In our design, the optimal distance between the absorbing TJ and the QWs is carefully adjusted to 28 nm in order to obtain the modal gain-loss balance. The polarization-engineered heterostructure TJ, used in the lasers, includes a 4 nm unintentionally doped (UID)-GaN layer which is sandwiched between a highly-doped p-AlGaN layer with Mg doping concentration of 5×10^{19} cm^{-3} and an n-AlGaN layer with Si doping concentration of 1×10^{20} cm^{-3} [23]. To compensate for the raised depletion

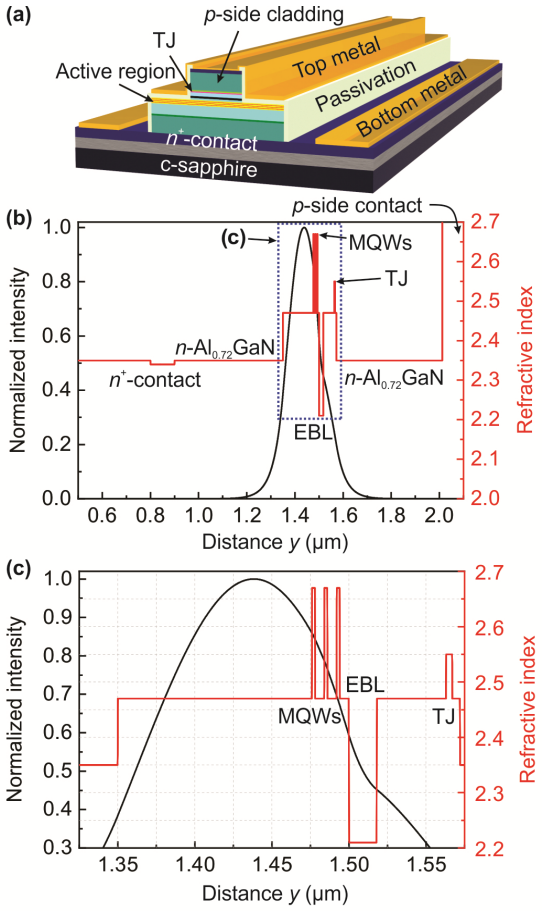

Fig. 2. (a) 3D schematic view of a fully-processed shallow-ridge laser, (b) 1D intensity distribution of the mode and refractive index profile in the transverse direction, where $n_{\text{eff}} = 2.42$ is the effective refractive index of the fundamental TE mode, and (c) a close-up view of the laser center, marked by a dotted blue rectangle in (b).

TABLE I
Calculated Γ Values for Several Sections of the Laser

Optical Mode in	Confinement Factor Γ (%)
Undoped 3 QWs	2.7
Top and Bottom cladding	13.6
Tunnel junction	0.55
Waveguide layer	59.7
p- and n- contact layers	1.6×10^{-4}

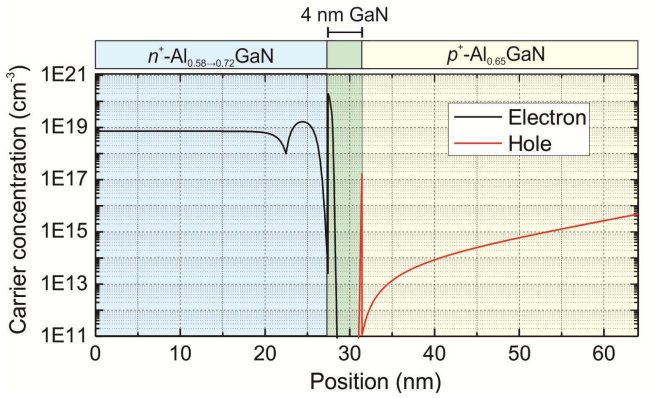

Fig. 3. Spatial carrier concentration profile across the tunnel junction used in the lasers.

barrier due to the large band offset between GaN and AlGaN, bulk polarization charges are introduced by incorporating a 5 nm thin grading layer at the end of the AlGaN layer followed by a thick 440 nm n-AlGaN layer. The strong polarization dipole generation at the GaN/AlGaN interface creates a sharp band alignment across the junction. The carrier concentration profile at equilibrium is shown in Fig. 3. At room-temperature, the Mg acceptor ionization energy is 424 meV for the 65% Al-containing layer and the Si donor ionization energy was fixed at 18 meV [23], [24]. Due to high ionization energy, the maximum hole concentration achieved in p-AlGaN:Mg was only on the order of 5×10^{15} cm^{-3} with a 2D hole gas at the GaN/p-AlGaN interface.

The optical absorption loss due to the polarization-engineered TJ with a non-transparent GaN interlayer may be high since the bandgap of GaN is much lower than the photon energy. In the ideal case, this GaN layer should be placed at the node of the optical mode [25] resulting in low optical absorption. This is, however, not possible for the edge-emitting laser design, where the buried TJ is used as an intracavity contact. In order to gauge suitability for such TJs within the device, it is important to know the absorption loss quantitatively. The free carrier absorption losses of the all the device layers except the GaN TJ interlayer were calculated and the values are listed in Table II. The free-carrier loss due to p-doped layers was negligible and therefore not listed. According to the Drude model, the free carrier loss can be calculated by [26]:

$$\alpha_{\mathrm{FC}} = \frac{q^3\lambda^2}{4\pi^2 c^3 \varepsilon_0 n}\left(\frac{N}{m_e^{*2}\mu_e} + \frac{P}{m_h^{*2}\mu_h}\right) \quad (1)$$

where c is the speed of light, ϵ_0 the dielectric constant, N and P the electron and hole concentrations, respectively, λ is the wavelength, μ the mobility, m the effective mass and α_{FC} the absorption coefficient. Using the material constants from literature [27]–[31] and equation (1), free carrier absorption coefficient of the TJ layers was calculated. Introduction of p-doped layers with Mg-dopants creates strong absorption tails near the material bandgap. Even for lower-Mg concentrations, the extension of the absorption tail to regions smaller than material bandgaps yields high Mg-induced modal losses. The absorption coefficient for Mg-doped $Al_{0.7}Ga_{0.3}N$ layers around the wavelength of interest was experimentally measured to be 50 cm^{-1} [32]. This allows the calculation of the optical losses for p-doped layers of the laser and enables to optimize its design by maintaining the internal loss within reasonable limits.

TABLE II
THE FREE CARRIER AND BAND-TO-BAND ABSORPTION DATA OF SEVERAL ABSORBING LAYERS AT A WAVELENGTH OF 290 NM

Layers	Γ (%)	α (cm^{-1})	Γα (cm^{-1})
n-$Al_{0.72}GaN$	4.6	2.6	0.1
n-$Al_{0.72\text{-}0.58}GaN$ graded	0.5	440	2.2
GaN	0.5	10^4 [30], [31]	55.1
p-$Al_{0.65}GaN$	12.4	50 [32]	6.2
AlN	2.5	50 [32]	1.3
n-$Al_{0.65}GaN$	57.2	2.7	1.5
n-$Al_{0.72}GaN$	8.9	2.6	0.2

It should be noted that the absorption loss due to the non-transparent ultra-thin GaN interlayer within the TJ considers a reported bulk absorption coefficient. This is valid for thick layers, but strained ultra-thin layers under a strong electric field subject to quantum confinement will possibly contribute to a reduced absorption loss in the device. As a matter of fact, the bulk absorption characteristics are, indeed, different from ultra-thin films due to a modification of the density of states as well as selection rules of occupation just as in any band-to-band gain/absorption calculation. Ultra-thin materials whose bandgap is smaller than the photon energy may become transparent if the upper quantized states are filled and non-resonant to the incident light, so that transitions due to band-to-band absorption are inhibited. In this case, free-carrier absorption dominates over the band-to-band transition.

Based on the modal absorption losses of all the device layers, the total loss value is calculated by $\alpha = (\alpha_{\mathrm{FC}} + \alpha_{\mathrm{b-b}})\Gamma$; where α_{FC} and $\alpha_{\mathrm{b-b}}$ are the absorption coefficient due to free carrier plasma effect and band-to-band transitions, respectively [33]. It can be seen from Table II that the total loss is dominated by the GaN interlayer and the resulting overestimated loss value of 84 cm^{-1} is considerably high with a mirror loss of 17.6 cm^{-1}. The higher internal loss of the resonator is mainly liable for a comparatively larger threshold current in the device. Therefore, an alternative low-resistive TJ design without a highly absorbing layer is required to obtain a loss value as low as < 20 cm^{-1} for the lasers.

IV. ELECTRICAL DESIGN

A. Tunnel Junction

A polarization-engineered heterostructure TJ is utilized in the designed lasers to achieve efficient hole injection through interband tunneling. In fact, the introduction of the GaN interlayer reduces the tunneling barrier which increases the hole injection efficiency to the active region. Despite careful placement of such a TJ with an ultra-thin GaN interlayer within the device, it is of utmost importance to achieve

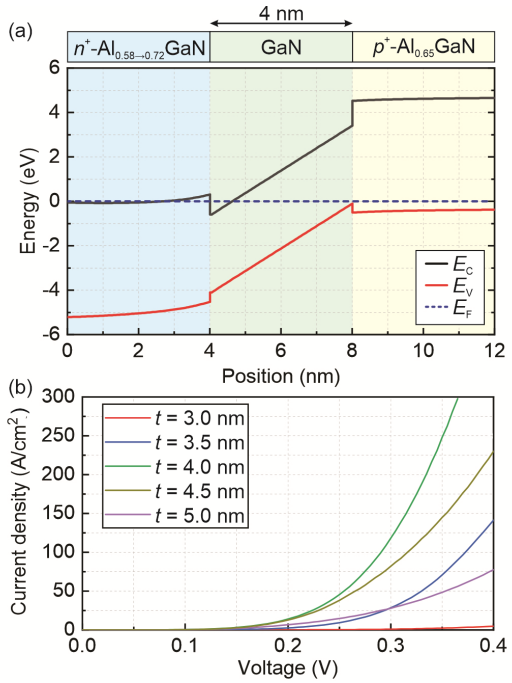

Fig. 4. Calculated (a) energy band diagram and (b) *I-V* characteristics of the standalone TJ buried in the lasers by varying the thickness of the GaN interlayer.

reasonably good electrical properties through the TJs. The band diagram of the TJ used in this study [34] is shown in Fig. 4(a). Due to the polarization discontinuity, sheet charges are formed at the interface by inserting a thin GaN layer between *n*- and *p*-doped $Al_xGa_{1-x}N$. The resulting 2D electron and hole gases enhance the carrier tunneling process and contribute to the tunneling current. Importantly, varying the thickness of the GaN interlayer is also found to affect the carrier tunneling probability. It turns out that an optimal thickness of the GaN interlayer is essential to realize good electrical performance in terms of a low voltage penalty at a given current.

Given that the TJs within the forward-biased devices operate in the reverse direction, Fig. 4(b) shows the calculated current-voltage (I–V) characteristics under reverse-bias for various GaN thicknesses. It is found that the 4 nm GaN interlayer shows the best I–V characteristics with some voltage penalty due to the non-zero tunneling barrier in the band diagram. The tunneling current is a function of tunneling probability and the number of available states on either side of the junction. For a thinner GaN layer, the sheet charges at the interface of GaN/$Al_xGa_{1-x}N$ decreases dramatically. Even though the tunneling rate is high, the tunneling current is lower. For the case of a thicker GaN interlayer, the low tunneling rate may dominate the tunneling process and cause a reduction in the tunneling current.

B. Laser Series Resistance

Calculating the series resistances of each layer and having an understanding of the total resistance of the laser is important since high series resistance often impedes the device operation in CW mode. The high silicon doping concentrations and the resulting equal electron density enabled by its low ionization energy results in a negligible resistance in the quasi-neutral *n*-regions. However, since the Mg acceptor exhibits high ionization energy, the equilibrium hole density is few orders of magnitude lower than the doping concentration. Consequently, 18 nm *p*-EBL and 10 nm *p*-waveguide layer contribute to a major portion of the series resistance. Due to the background doping concentration of a growth reactor, the hole concentration of the *p*-doped layers can vary. Fig. 5 presents the calculated total series resistance of the laser as a function of the hole concentration.

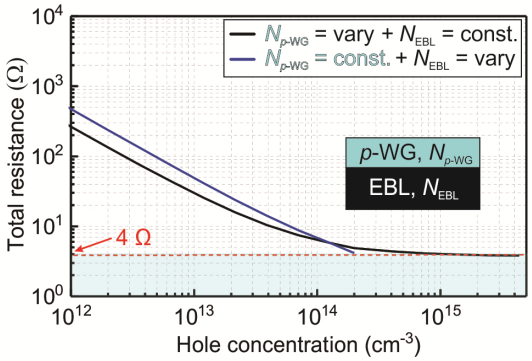

Fig. 5. Calculated series resistance of the diode laser as a function of the *p*-doped materials in the laser structure. The both *p*-doped EBL and waveguide layers are assumed to have a constant hole concentration of 10^{14} cm^{-3} at room-temperature.

The equilibrium hole concentration of the *p*-$Al_{0.65}GaN$ (black) and *p*-AlN (blue) at room-temperature was varied from 10^{12} to 5×10^{15} cm^{-3} and 10^{12} to 2×10^{14} cm^{-3}, respectively for an Mg doping concentration of 5×10^{19} cm^{-3}. The upper limit of the hole concentrations in the *p*-waveguide and EB layers are defined by the high activation energies of Mg acceptors. Hence, the total series resistance of the device is calculated to be 4 Ω by assuming hole concentrations of 10^{14} cm^{-3} and 5×10^{14} cm^{-3} in the EBL and *p*-waveguide layer, respectively. Note that the buried TJ, allowing to replace thick and high Al-content *p*-materials by the *n*-doped layers, reduces series resistance in the devices which also eventually provides a better thermal management by reducing Joule heating. For example, a threshold current density of 6 kA/cm^2 for a 400-nm-thick *p*-AlGaN layer requires a threshold voltage of over 200 V as opposed to less than 4 V for TJ-based devices.

V. Thermal Design

The theoretical thermal analysis of the AlGaN-based FP laser was performed using finite element methods. A 2D, laterally symmetric, steady-state heat transfer model was designed, by assuming a uniform heat source in the active region of the laser. Owing to the dominance of the *n*-type layers in the laser structure, Joule-heating from the highly resistive AlN EBL and *p*-AlGaN waveguide layers, with a total thickness of only 28 nm, was neglected. In fact, the applied electrical power at threshold over these two resistive regions is a factor of five less compared to the active region, justifying the localization of the heat source in the active region. The sapphire substrate is in contact with a copper heat sink maintained at a constant

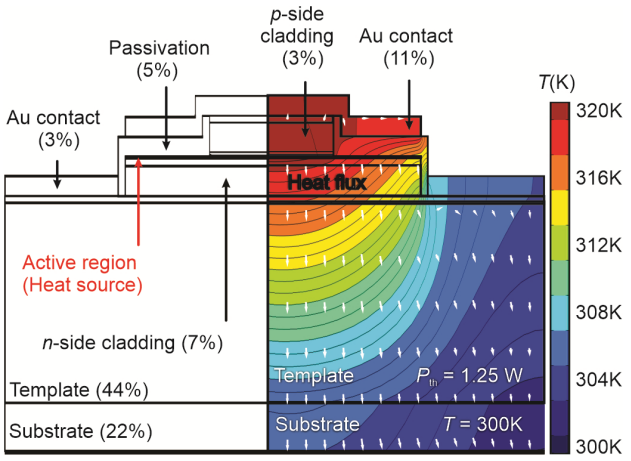

Fig. 6. The geometric layered structure of the episide-up AlGaN lasers showing the contribution from different layers towards heat dissipation (left), and heat flux contours in the laser structure (right). The substrate bottom is maintained at a temperature of 300 K by a heat sink (not shown) whose dimension is large compared to the device dimensions.

temperature of 300 K. Natural convection with air is considered for the outer surface of the entire stack except the heat sink.

A 2D profile of the temperature distribution within the laser diode was determined using the heat balance equation using the finite element method. Thermal conductivities of the various layers in the laser structure were taken from [26], [35], and [36]. The effect of anisotropy in the thermal conductivities [37] of the materials used is negligible and do not contribute to any noticeable variations in the result. The heat dissipation in the active region was modeled at a threshold current. Since the wall-plug efficiency is nearly zero at threshold, all the applied electric power is assumed to be dissipated as heat.

Fig. 6 presents the isothermal contour plot obtained from the simulation, showing most of the heat localized in the *p*-side. The white arrows in the diagram indicate the direction of the heat flux. Around 80% of the heat is dissipated via the layers on the *n*-side, in contact with the substrate and the heat sink. Though the percentage of total energy transferred to the *p*-side is comparatively lower due to the presence of passivation layers with low thermal conductivity, the negligible natural convection at the Au-air interface leads to an increase in the temperature on the *p*-side. With respect to the materials used in the different layers, AlN has a comparatively higher thermal conductivity, and ternary compounds with larger mole fractions of Al exhibit lower κ values [36]. This is apparent in the heat dissipation seen in the $Al_{0.72}GaN$ template layer on the *n*-side. The sapphire substrate owing to its low κ contributes to an increase in the thermal resistance by reducing the rate of outflow of heat from the entire structure. The thermal impedance (Z_t) of the laser is calculated to be 16 K/W.

Efficient thermal management is one of the key figures of merit for diode lasers. In order to sustain in a practical integrated system, especially, in high power applications, a lower Z_t is a prerequisite. For improving the heat dissipation of the same laser structure, an episide-down mounted device

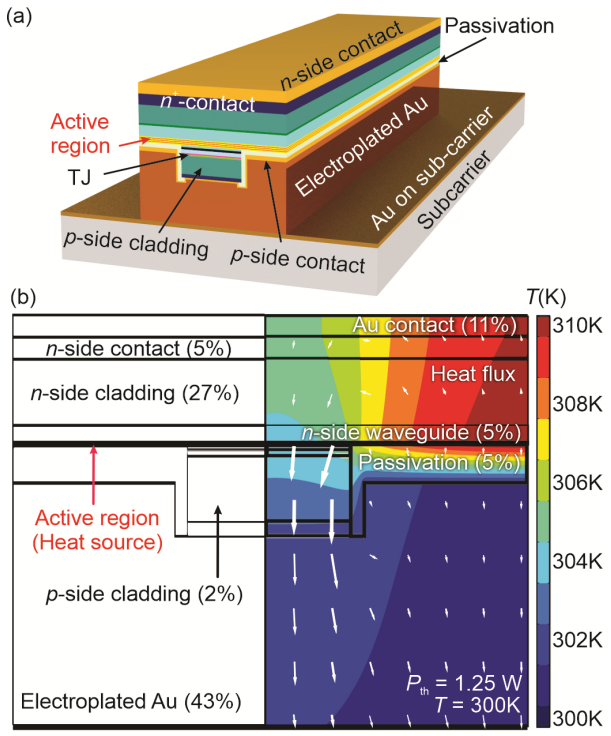

Fig. 7. (a) Schematic of the episide-down mounted device, and (b) the corresponding heat flux contours at laser threshold. A better heat distribution is observed due to larger area of Au bottom contact. Consequently, Z_t is reduced in comparison to the episide-up configuration, paving the way to better performance in CW mode.

with an integrated Au heat sink [38] was also simulated. The device schematic and the corresponding thermal profile are shown in Fig. 7(a) and (b), respectively. As can be seen that the heat generating active region is now much closer to the highly conductive Au-contact. As a result, most of the heat generated is effectively dissipated in the *p*-side of the device via the Au-contact. The wider area of the Au heat sink also improves heat spreading compared to the previously presented narrow-ridge structure of the epi-up device. A small rise in the active area temperature is seen in case of the episide-down mounted device. Consequently, Z_t of 8 K/W is calculated for the device.

A close comparison in terms of thermal management with typical AlGaN laser diodes in existing literature reveals the significance of the achieved results. For AlGaN laser diodes with episide up and down mounted configurations, a Z_t value of 20-80 K/W has been reported [39], [40]. In a typical *p-i-n* configured, FP III-nitride laser, the thick and resistive *p*-doped layers contribute to heat generation outside the active region. However, in our device structure, the presence of the TJ eliminates the *p*-doped layers and the accompanying large series resistance, leading to improved thermal performance. Self-heating is one of the major setbacks to achieving low-threshold CW operation in a laser. A reduced thermal impedance in our UV laser design helps overcome this issue. Different strategies including diamond heat spreader and microchannel cooling [41], [42] are usually adopted to achieve lower thermal impedance in the device. However, an integrated on-chip

approach to lower the value of Z_t is more appealing as it leads to simple and efficient designs.

VI. AlGaN Laser Performance Analysis

In order to model the EP lasers, the threshold current of the lasers was calculated, and their output characteristics were determined using the values of Z_t, obtained in Section V.

A. Threshold Current

The threshold of the shallow-ridge laser was first calculated for the designed structure. Due to lower material gain achievable from the AlGaN materials, index guiding is essential to obtain lasing from these devices. A standard LD of 1 mm length (L) and 5 μm ridge width (w) was considered for the calculation of threshold current. Considering internal loss $\alpha_i = 66$ cm^{-1} and a mirror loss value of $\alpha_m = 17.4$ cm^{-1}, with a mirror reflectivity of 0.175 for naturally cleaved facets, a total loss of 84 cm^{-1} was calculated. The calculated average internal loss for the UV-B lasers is considered reasonable by comparing with the values ranging from 55–75 cm^{-1}, reported for UV-A and blue lasers [43], [44]. A higher transparency carrier density was assumed (N_{tr}) in comparison to typical UV-A lasers based on the quality of the grown material [10].

Since there are no reports of EP UV-B lasers at this wavelength, a gain coefficient g_0 of 6000 cm^{-1} is assumed [45]. The threshold current I_{th} is related to the carriers under steady state by the rate equation [46].

$$\frac{\eta_i I_{th}}{q V_a} = A N_{th} + B N_{th}^2 + C N_{th}^3$$

where A, B, and C represent the Shockley–Read–Hall (SRH) nonradiative, bimolecular radiative, and the Auger nonradiative recombination parameters, respectively. Given the poorer quality of grown material compared to well established UV-A and blue lasers, the value of A, B and C was taken to be 1×10^8 /s [10], 3×10^{-12} cm^3/s [47] and 10^{-30} cm^6/s [48]. Similarly, the injection efficiency η_i is assumed to be 60% due to the 18 nm EBL, consisting of p-AlN, effectively blocking the overflow of excess carriers. A precise calculation of the injection efficiency is challenging due to interplay of many processes. In practice, one of the main causes of a reduced η_i value for a typical QW laser is the recombination of carriers in the undoped or weakly-doped waveguide regions, which can vary with bias, up to threshold.

Shockley–Read–Hall lifetime and Auger recombination coefficients also strongly influence the threshold current. Considering these parameters and plugging them into the rate equation results in a threshold current of ~290 mA for the designed laser, yielding a threshold current density of 5.8 kA/cm^2. From the parameters stated above, the calculated differential quantum efficiency of the laser is around 12%. It is noted here that the threshold current density of the III-nitride based CW-lasers emitting at blue wavelengths has reached around 2 kA/cm^2 due to a rapid advancement in material growth techniques [49].

B. Output Characteristics

Using the calculated threshold current and differential quantum efficiency values, the light output power P vs current I characteristic of the lasers are determined. This represents the pulsed P-I characteristics of the device, typically showing a linear profile above threshold. To construct the CW P-I characteristics, Joule heating in the device was considered by employing the characteristic temperature values taken from [50]. For the devices with an episide-up geometry, the CW threshold current is as high as 410 mA and can be explained by poor thermal management. This can be understood by a high temperature change (ΔT) and an associated change in conversion efficiency with current, as shown in Fig. 8(a).

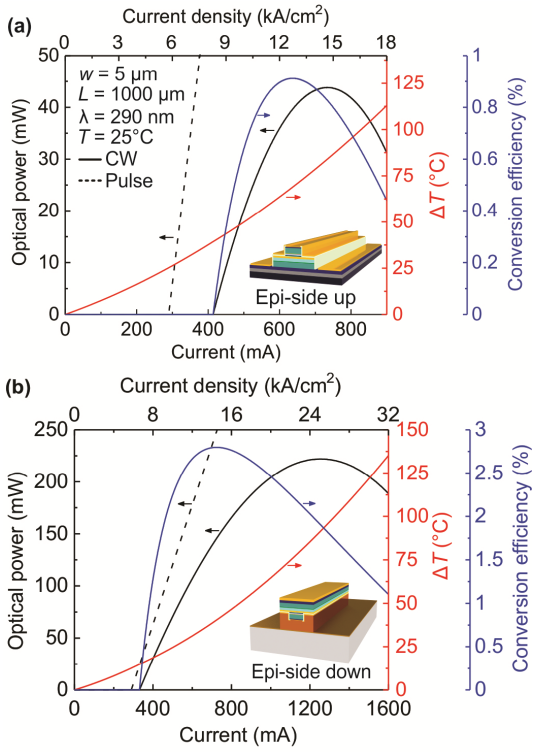

Fig. 8. Numerically calculated output characteristics for CW and pulsed operation, as well as temperature rise and conversion efficiency versus current for the laser devices with (a) episide-up and (b) episide-down geometries.

With increasing input power, there is a rise in conversion efficiency but after a certain point, most of the injected power is converted into heat, leading to a reduction in output power. In our design, a maximum, conversion efficiency of 0.9% was reached for the epi-up devices. On the contrary, Joule heating is minimized in episide-down-mounted lasers with the Au heat sink, leading to better thermal management of the devices. The novel episide-down mounting helps to conduct heat more efficiently from the active region to the heat sink, enabling CW operation at higher current. Finally, the calculated CW threshold current and maximum conversion efficiency for this structure is ~330 mA and 2.8%, respectively, as shown in Fig. 8(b).

C. Ridge Height

The height of III-nitride ridge waveguides, defined by dry etching during device fabrication, influences the optical field

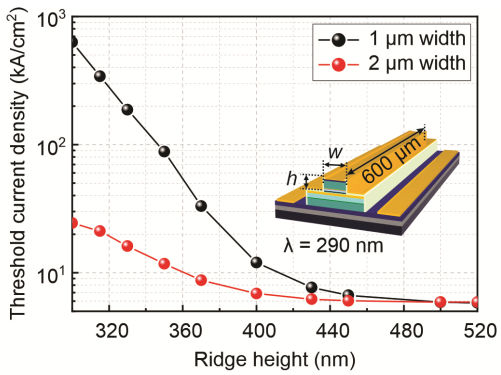

Fig. 9. The dependence of calculated threshold current density on ridge height h for shallow-ridge devices.

distribution. The effective refractive index difference Δn_{eff} in the lateral direction, between the ridge waveguide and the etched region, increases with h, yielding a higher lateral confinement factor. In other words, lateral optical confinement provided by Δn_{eff} is enhanced by increasing h. As a standard practice, surface effects can be minimized if barriers are provided that are ~30 nm thick. By taking this into account, one should ideally stop the etching ~30 nm above from the QWs to define shallow ridges. Hence, an optimized value of h leads to reduced etch damage in the active region and higher lateral confinement factor can then be ensured. In order to obtain strong index guiding, the ideal ridge height for such AlGaN lasers should be selected as the sum of thickness of the TJ, EBL, n-AlGaN cladding layer and the top n-AlGaN contact layer.

Unfortunately, there are no reliable and selective dry etching techniques which could allow the control of the ridge height precisely. As a result, a change in the ridge-height caused by a variation of the process or etch system from one fabrication run to another is frequently observed. Fig. 9 shows the dependence of threshold current density on the ridge height for a given cavity length. The threshold current density for UV LDs with widths of 1 μm and 2 μm is calculated by varying the ridge height. Nearly all the optical power in QW layers is confined in the core region, which implies a significant decrease in internal loss and threshold current. As shown in Fig. 9, the threshold current density will no longer vary between the two devices when the height is designed to be larger than around 450 nm. The threshold current decreases with increasing h as predicted by the simulation results.

Considering the single-mode condition and assuming no optical loss, the maximum width of a surface ridge waveguide for the AlGaN laser can be calculated to be ~0.6 μm. This suggests that lasers at 290 nm, with $w \geq 0.6$ μm, are expected to support multiple transverse modes. But experimentally, devices with larger widths (compared to the values estimated here) are observed to emit a single fundamental mode. As a matter of fact, single-mode lasers may have a lateral waveguide width that supports multiple modes but only the fundamental mode lases. The reason behind this is mode-selective loss and gain in the cavity. In other words, the net losses for the higher order modes are greater, and the net gain for the fundamental mode is larger than for the other modes, ensuring single mode operation.

VII. Conclusion

We have designed EP AlGaN MQW lasers emitting at sub-300 nm with CW threshold current densities of less than 8 kA/cm^2. For efficient hole injection through interband tunneling, ultra-wide bandgap AlGaN-based and polarization engineered TJs are employed in the devices. The proposed TJ-based device concept also allows achieving an excellent thermal management in the devices, paving the way to CW-operating lasers. This is clearly a significant step forward towards demonstrating first EP and CW-operating lasers in this critical wavelength regime. However, developing and demonstrating low-resistive and low-absorptive interlayer-free TJs leave a big room for potential improvement in terms of reducing threshold current density even further, yielding improved device characteristics. As a part of the investigation, II-IV-N_2 homojunctions and III-N – II-IV-N_2 heterojunctions are potential candidates to explore which can be integrated in AlGaN based optoelectronic devices [51]. Boron containing III-nitride alloys are another promising TJ material candidates which is also worth investigating [52].

References

[1] S. Vilhunen, H. Särkkä, and M. Sillanpää, "Ultraviolet light-emitting diodes in water disinfection," *Environ. Sci. Pollut. Res.*, vol. 16, no. 4, pp. 439–442, Feb. 2009.

[2] T. Wunderer, J. E. Northrup, and N. M. Johnson, *AlGaN-Based Ultraviolet Laser Diodes*. Cham, Switzerland: Springer, 2015.

[3] Z. Bryan, I. Bryan, R. Kirste, R. Collazo, and Z. Sitar, "Status and challenges in deep UV semiconductor lasers," in *Proc. IEEE Summer Topicals Meeting Ser. (SUM)*, Jul. 2015, pp. 123–124.

[4] J. Wallace. (2020). *Seoul Viosys Sees Increased Demand for its UV LEDs for Sterilization to Prevent Spread of Corona Virus*. Accessed: May 22, 2020. [Online]. Available: https://www.laserfocusworld.com/lasers-sources/article/14169058/seoul-viosys-sees-increased-demand-for-its-uv-leds-for-sterilization-to-prevent-spread-of-coronavirus

[5] S. Arafin, X. Liu, and Z. Mi, "Review of recent progress of III-nitride nanowire lasers," *J. Nanophoton.*, vol. 7, no. 1, Sep. 2013, Art. no. 074599.

[6] M. Nakarmi *et al.*, "Electrical and optical properties of Mg-doped Al0.7Ga0.3N alloys," *Appl. Phys. Lett.*, vol. 86, no. 9, Feb. 2005, Art. no. 092108.

[7] Z. Zhang *et al.*, "A 271.8 nm deep-ultraviolet laser diode for room temperature operation," *Appl. Phys. Express*, vol. 12, no. 12, Nov. 2019, Art. no. 124003.

[8] M. Martens *et al.*, "Low absorption loss p-AlGaN superlattice cladding layer for current-injection deep ultraviolet laser diodes," *Appl. Phys. Lett.*, vol. 108, no. 15, Apr. 2016, Art. no. 151108.

[9] S. Arafin, S. M. N. Hasan, Z. Jamal-Eddine, D. Wickramaratne, B. Paul, and S. Rajan, "Design of AlGaN-based lasers with a buried tunnel junction for sub-300 nm emission," *Semicond. Sci. Technol.*, vol. 34, no. 7, Jun. 2019, Art. no. 074002.

[10] H. Yoshida, Y. Yamashita, M. Kuwabara, and H. Kan, "Demonstration of an ultraviolet 336 nm AlGaN multiple-quantum-well laser diode," *Appl. Phys. Lett.*, vol. 93, no. 4, pp. 241106–241109, Nov. 2008.

[11] H. Yoshida, Y. Yamashita, M. Kuwabara, and H. Kan, "A 342-nm ultraviolet AlGaN multiple-quantum-well laser diode," *Nature Photon.*, vol. 2, no. 9, pp. 551–554, Jul. 2008.

[12] C. Reich *et al.*, "Strongly transverse-electric-polarized emission from deep ultraviolet AlGaN quantum well light emitting diodes," *Appl. Phys. Lett.*, vol. 107, no. 14, Oct. 2015, Art. no. 142101.

[13] K. Sato *et al.*, "Light confinement and high current density in UVB laser diode structure using al composition-graded p-AlGaN cladding layer," *Appl. Phys. Lett.*, vol. 114, no. 19, May 2019, Art. no. 191103.

[14] X.-H. Li *et al.*, "Demonstration of transverse-magnetic deep-ultraviolet stimulated emission from AlGaN multiple-quantum-well lasers grown on a sapphire substrate," *Appl. Phys. Lett.*, vol. 106, no. 4, Jan. 2015, Art. no. 041115.
[15] C. Chu *et al.*, "On the origin of enhanced hole injection for AlGaN-based deep ultraviolet light-emitting diodes with AlN insertion layer in p-electron blocking layer," *Opt. Express*, vol. 27, no. 12, p. A620, Jun. 2019.
[16] H. Hirayama, "Growth of high-quality AlN on sapphire and development of AlGaN-based deep-ultraviolet light-emitting diodes," in *Semiconductor Semimet*, vol. 96. Amsterdam, The Netherlands: Elsevier, 2017, pp. 85–120.
[17] Y. Chriqui *et al.*, "Direct growth of GaAs-based structures on exactly (001)-oriented Ge/Si virtual substrates: Reduction of the structural defect density and observation of electroluminescence at room temperature under CW electrical injection," *J. Cryst. Growth*, vol. 265, nos. 1–2, pp. 53–59, Apr. 2004.
[18] I. S. Bryan, "Al-rich AlGaN and AlN growth on bulk AlN single crystal substrates," Ph.D. dissertation, Mater. Sci. Eng., North Carolina State University, Raleigh, CA, USA, 2015.
[19] T.-Y. Wang, C.-T. Tasi, C.-F. Lin, and D.-S. Wuu, "85% internal quantum efficiency of 280-nm AlGaN multiple quantum wells by defect engineering," *Sci. Rep.*, vol. 7, no. 1, Oct. 2017, Art. no. 14422.
[20] S. Neugebauer *et al.*, "All metalorganic chemical vapor phase epitaxy of p/n-GaN tunnel junction for blue light emitting diode applications," *Appl. Phys. Lett.*, vol. 110, no. 10, Mar. 2017, Art. no. 102104.
[21] J. Wang *et al.*, "Hybrid III-nitride tunnel junctions for low excess voltage blue LEDs and UVC LEDs," in *Proc. Compound Semiconductor Week (CSW)*, May 2019, p. 1.
[22] E. A. Clinton *et al.*, "Negative differential resistance in GaN homojunction tunnel diodes and low voltage loss tunnel contacts," *Appl. Phys. Lett.*, vol. 112, no. 25, Jun. 2018, Art. no. 252103.
[23] B. Borisov *et al.*, "Si-doped $Al_xGa_{1-x}N(0.56\leq \times \leq 1)$ layers grown by molecular beam epitaxy with ammonia," *Appl. Phys. Lett.*, vol. 87, no. 13, Sep. 2005, Art. no. 132106.
[24] K. B. Nam, M. L. Nakarmi, J. Li, J. Y. Lin, and H. X. Jiang, "Mg acceptor level in AlN probed by deep ultraviolet photoluminescence," *Appl. Phys. Lett.*, vol. 83, no. 5, pp. 878–880, Aug. 2003.
[25] V. Fan Arcara, B. Damilano, G. Feuillet, A. Courville, S. Chenot, and J.-Y. Duboz, "(Ga,In)N/GaN light emitting diodes with a tunnel junction and a rough n-contact layer grown by metalorganic chemical vapor deposition," *AIP Adv.*, vol. 9, no. 5, May 2019, Art. no. 055101.
[26] A. Tomczyk, R. P. Sarzala, T. Czyszanowski, M. Wasiak, and W. O. Nakwaski, "Fully self-consistent threshold model of one-dimensional arrays of edge-emitting nitride diode lasers," *Semicond. Sci. Technol.*, vol. 19, no. 8, pp. 997–1004, Jun. 2004.
[27] T. D. Moustakas, "Ultraviolet optoelectronic devices based on AlGaN alloys grown by molecular beam epitaxy," *MRS Commun.*, vol. 6, no. 3, pp. 247–269, Sep. 2016.
[28] M. Miyoshi *et al.*, "MOVPE growth and characterization of high-Al-content AlGaN/GaN heterostructures on 100-mm-diameter sapphire substrates," *J. Cryst. Growth*, vol. 272, nos. 1–4, pp. 293–299, Dec. 2004.
[29] S. Rajan, S. P. DenBaars, U. K. Mishra, H. Xing, and D. Jena, "Electron mobility in graded AlGaN alloys," *Appl. Phys. Lett.*, vol. 88, no. 4, Jan. 2006, Art. no. 042103.
[30] O. Ambacher, W. Rieger, P. Ansmann, H. Angerer, T. D. Moustakas, and M. Stutzmann, "Sub-bandgap absorption of gallium nitride determined by photothermal deflection spectroscopy," *Solid State Commun.*, vol. 97, no. 5, pp. 365–370, Feb. 1996.
[31] Y. Zhang, Z.-F. Wu, P.-F. Gao, D.-Q. Fang, and S.-L. Zhang, "Enhanced visible light absorption in ZnO/GaN heterostructured nanofilms," *J. Alloys Compounds*, vol. 704, pp. 478–483, May 2017.
[32] M. Martens *et al.*, "The effects of magnesium doping on the modal loss in AlGaN-based deep UV lasers," *Appl. Phys. Lett.*, vol. 110, no. 8, Feb. 2017, Art. no. 81103.
[33] L. Q. Zhang *et al.*, "Confinement factor and absorption loss of AlInGaN based laser diodes emitting from ultraviolet to green," *J. Appl. Phys.*, vol. 105, no. 2, Jan. 2009, Art. no. 023104.
[34] C. Kuhn *et al.*, "MOVPE-grown AlGaN-based tunnel heterojunctions enabling fully transparent UVC LEDs," *Photon. Res.*, vol. 7, no. 5, p. B7, May 2019.
[35] B. N. Pantha *et al.*, "Thermoelectric properties of In0.3Ga0.7N alloys," *J. Electron. Mater.*, vol. 38, no. 7, pp. 1132–1135, Feb. 2009.
[36] W. Liu and A. A. Balandin, "Temperature dependence of thermal conductivity of $Al_xGa_{1-x}N$ thin films measured by the differential 3ϖ technique," *Appl. Phys. Lett.*, vol. 85, no. 22, pp. 5230–5232, Nov. 2004.
[37] M. Osiáski and W. Nakwaski, "Effective thermal conductivity analysis of 1.55 μm InGaAsP/InP vertical-cavity top-surface-emitting microlasers," *Electron. Lett.*, vol. 29, no. 11, pp. 1015–1016, May 1993.
[38] E. Vadiee *et al.*, "The role of Mg bulk hyper-doping and delta-doping in low-resistance GaN homojunction tunnel diodes with negative differential resistance," *J. Appl. Phys.*, vol. 126, no. 8, Aug. 2019, Art. no. 083110.
[39] G. Hatakoshi *et al.*, "Thermal analysis for GaN laser diodes," *Jpn. J. Appl. Phys.*, vol. 38, no. 5, pp. 2764–2768, May 1999.
[40] W. Joon Hwang *et al.*, "Thermal investigation of GaN-based laser diode package," *IEEE Trans. Compon. Packag. Technol.*, vol. 30, no. 4, pp. 637–642, Dec. 2007.
[41] D. Lorenzen *et al.*, "Micro thermal management of high-power diode laser bars," *IEEE Trans. Ind. Electron.*, vol. 48, no. 2, pp. 286–297, Apr. 2001.
[42] T. Åwietlik *et al.*, "Anomalous temperature characteristics of single wide quantum well InGaN laser diode," *Appl. Phys. Lett.*, vol. 88, no. 7, Feb. 2006, Art. no. 071121.
[43] K. Kojima *et al.*, "Gain suppression phenomena observed in $In_xGa_{1-x}N$ quantum well laser diodes emitting at 470nm," *Appl. Phys. Lett.*, vol. 89, no. 24, Dec. 2006, Art. no. 241127.
[44] E. Kioupakis, P. Rinke, and C. G. Van de Walle, "Determination of internal loss in nitride lasers from first principles," *Appl. Phys. Express*, vol. 3, no. 8, Jul. 2010, Art. no. 082101.
[45] G. Yuan, K. Xiong, C. Zhang, Y. Li, and J. Han, "Optical engineering of modal gain in a III-nitride laser with nanoporous GaN," *ACS Photon.*, vol. 3, no. 9, pp. 1604–1610, Aug. 2016.
[46] L. A. Coldren, S. W. Corzine, and M. L. Mashanovitch, *Diode Lasers and Photonic Integrated Circuits*. New York, NY, USA: Wiley, 2012.
[47] A. David, N. G. Young, C. Lund, and M. D. Craven, "Review—The physics of recombinations in III-nitride emitters," *ECS J. Solid State Sci. Technol.*, vol. 9, no. 1, Jan. 2020, Art. no. 016021.
[48] J. Verma, S. Islam, A. Verma, V. Protasenko, and D. Jena, "Nitride LEDs based on quantum wells and quantum dots," in *Nitride Semiconductor Light-Emitting Diodes*, 2nd ed. Amsterdam, The Netherlands: Elsevier, 2018, pp. 377–413.
[49] T. Kamikawa *et al.*, "Realization of thin-film m-plane InGaN laser diode fabricated by epitaxial lateral overgrowth and mechanical separation from a reusable growth substrate," *Opt. Express*, vol. 27, no. 17, pp. 24717–24723, Aug. 2019.
[50] H. Yoshida, M. Kuwabara, Y. Yamashita, Y. Takagi, K. Uchiyama, and H. Kan, "AlGaN-based laser diodes for the short-wavelength ultraviolet region," *New J. Phys.*, vol. 11, no. 12, Dec. 2009, Art. no. 125013.
[51] W. R. L. Lambrecht and A. Punya, *Heterovalent Ternary II-IV-N_2 Compounds: Perspectives for a New Class of Wide-band-gap Nitrides within III-Nitride Semiconductors and Their Modern Devices* (Semiconductor Science and Technology). Oxford, U.K.: Oxford Univ. Press, 2013.
[52] X. Li *et al.*, "100 nm thick single phase wurtzite BAlN films with boron contents over 10%," *Phys. Stat. Sol. B*, vol. 254, Jan. 2017, Art. no. 1600699.

Riazul Arefin received the B.S. degree from the Islamic University of Technology, Gazipur, Bangladesh, and the M.S. degree from École Normale Supérieure Paris-Saclay, Cachan, France. He is currently pursuing the Ph.D. degree with Electrical and Computer Engineering Department, The Ohio State University. His research interests include silicon photonics, nanophotonics, and optoelectronics.

Weicheng You was born in Sichuan, China. He received the B.S. degree in electronics engineering from Sichuan University, Sichuan, China, in 2017, and the M.S. degree in electrical engineering from The Ohio State University, Columbus, OH, USA, in 2019, where he is currently pursuing the Ph.D. degree.

Sujit H. Ramachandra received the B.E. degree from the R. V. College of Engineering, Bengaluru, India. He is currently pursuing the M.S. degree in electrical and computer engineering with The Ohio State University, as a part of the OPREL Laboratory. His research interests include silicon photonics, and lasers and integrated optics.

Syed M. N. Hasan was born in Dhaka, Bangladesh. He received the B.S. degree in materials and metallurgical engineering from the Bangladesh University of Engineering and Technology, Dhaka, Bangladesh, in 2012, and the M.S. degree in materials science and engineering from the Gwangju Institute of Science and Technology, Gwangju, South Korea, in 2015. He is currently pursuing the Ph.D. degree with Electrical and Computer Engineering Department, The Ohio State University.

Hyemin Jung was born in Daegu, South Korea. She is currently a member of Optics and Photonics Research Laboratory, Electrical and Computer Engineering Department, The Ohio State University. Her research interests include nanofabrication, photonics sensors, photonic integrated circuits, high-power semiconductor laser, and optoelectronics.

Mohammad Awwad received the bachelor's and master's degree in biomedical engineering from MTC, Cairo, Egypt. He is currently pursuing the Ph.D. degree in III–V semiconductors with the Electrical and Computer Engineering Department, The Ohio State University. His research focused on the fabrication of III–V semiconductors thin films. He joined the Optics and Photonics Research Laboratory in January 2020.

Shamsul Arafin (Senior Member, IEEE) is currently working as an Assistant Professor with Electrical and Computer Engineering Department, The Ohio State University. He has 12 years of experiences on the design, fabrication of widely tunable semiconductor lasers, including vertical-cavity surface emitting lasers (VCSELs). Over the last decade or so, his research interests center around III–V compound semiconductor nanotechnology for materials and devices: molecular beam epitaxial growth and characterization of thin films (and nanoscale) materials as well as realization of novel optoelectronic devices.